

# Double-Shell Carbon-Coated CoFe Alloy Nanoparticles Derived From Dopamine-Coated Prussian Blue Analogues for High-Efficiency Lithium-Sulfur Batteries

Huipeng Zhao<sup>1,\*</sup>, Jiao Tian<sup>2</sup>, Hongfang Jiu<sup>2</sup>, Qianwen Xu<sup>2</sup>, Congli Wang<sup>2</sup>, Sicong Che<sup>2</sup>, Zhixin Guo<sup>1</sup>, Lixin Zhang<sup>1,3</sup>

<sup>1</sup> School of Chemical Engineering and Technology, North University of China, Taiyuan 030051, People's Republic of China

<sup>2</sup> School of Science, North University of China, Taiyuan 030051, People's Republic of China

<sup>3</sup> Shanxi Key Laboratory of High Performance Battery Materials and Devices, North University of China, Taiyuan, 030051, People's Republic of China

\*E-mail: [zbdxzhaohuipeng@126.com](mailto:zbdxzhaohuipeng@126.com)

Received: 28 June 2022 / Accepted: 25 August 2022 / Published: 10 October 2022

In this study, we applied polydopamine (PDA) to the surface of the CoFe-PBA nanocube and named it CoFe-PBA@PDA. Subsequently, we calcinated the CoFe-PBA@PDA nanocube at 500°C for 3 h to obtain a double-shell carbon-coated CoFe nanoparticle (CoFe@C). Finally, we synthesized the CoFe@C/S composite material by diffusing sulfur into the host material, which is commonly used as a cathode material for lithium-sulfur (Li-S) batteries. Through chemisorption, polysulfides were captured by CoFe nanoparticles, and the electronic linkage between different components increased. The CoFe@C/S material had a high sulfur content (59%) and a capacity of up to 568.6 mAhg<sup>-1</sup> after 100-time cycles at 0.1 C. Also, it could maintain a capacity of 311.1 mAhg<sup>-1</sup> after 100 cycles at 0.5 C. The results showed that the designed composite material could significantly increase the electrochemical property of Li-S batteries.

**Keywords:** CoFe-Prussian blue analogue, Double-shell carbon, Lithium-sulfur battery, PDA

## 1. INTRODUCTION

Sulfur is less expensive, nontoxic and natural [1-2]. Moreover, a lithium-sulfur battery has the advantage of potential energy storage, and is expected to be a promising energy storage devices. However, at present, the way to the commercialization of this battery is hindered by the following three problems: (1) a low utilization rate of active substances results from the insulation of sulfur and the poor electrical conductivity of Li<sub>2</sub>S and Li<sub>2</sub>S<sub>2</sub> (2) The shuttle effect due to the dissolution of polysulfide in the

course of charging and discharging. (3) The density change between  $\text{Li}_2\text{S}$  and sulfur results in sulfur volume expansion[3-5]. In conclusion, some materials need to be designed to capture polysulfide in physical restriction and chemical anchoring.

To solve the aforementioned technical problems, it is imperative to select controllable nonpolar conductive carbon as the main body of sulfur material [6], which has high conductivity, large specific surface area, and large porosity. However, the material can only capture polysulfide physically because of its weak affinity with polysulfide, and cannot solve the shuttle effect triggered by the dissoluteness of polysulfide. Therefore, some polar substances are needed, including heterogeneously doped conductive carbon materials [7] and polar oxides, sulfides, and other metal compounds [8]. However, substances with strong adsorption to polysulfide cannot always show excellent electrochemical performance, which is because some of them can produce slow polysulfide conversion kinetics. As previously reported, some polar materials can adsorb polysulfide well, such as metal oxides ( $\text{TiO}_2$  [9-10],  $\text{MnO}_2$  [11],  $\text{Ti}_4\text{O}_7$  [12],  $\text{Fe}_2\text{O}_3$  [13],  $\text{Co}_3\text{O}_4$  [14], and  $\text{SnO}_2$  [15]), metal carbides ( $\text{TiC}$  [16],  $\text{NbC}$  [17], and  $\text{W}_2\text{C}$  [18]), metal hydroxides ( $\text{Ni}(\text{OH})_2$  [19]), metal nitrides ( $\text{VN}$  [20-21],  $\text{TiN}$  [22], and  $\text{Co}_4\text{N}$  [23]), metal sulfide ( $\text{CoS}_2$  [24],  $\text{WS}_2$  [25-26],  $\text{MoS}_{2-x}$  [27],  $\text{ZnS}$  [28], and  $\text{CoS}$  [29]), metal borides ( $\text{MgB}_2$  [30] and  $\text{TiB}_2$  [31]), and so forth. At present, researchers often use sulfides, polar metal oxides and heteroatom-doped conductive carbon materials to enhance the polarity of the entire material.

Currently, carbon has been come into common use in the cathode materials of Li-S batteries owing to its higher specific surface area and stronger conductivity. Nevertheless, it has a serious aggregation that hinders the entrance and migration of ions [32]. Therefore, the key to solving the problem is to find a suitable cathode material. Researchers found that Prussian blue materials with Lewis acid characteristics could interact strongly with polysulfides and capture them to the main body through a metal-sulfur bond [33]. The Prussian analogues not only have a stable structure, large lattice voids, simple preparation, and high theoretical capacity but also can promote Li-ion transfer and inhibit polysulfide dissolution owing to the suitable pore size and open structure. However, as an Metal-Organic Frameworks(MOF) material, poor conductivity has an influence on its electrochemical performance, leading to a low coulomb efficiency and a poor cycle [34].

Therefore, we synthesized the alloy particles coated with the double-shell carbon and diffused sulfur into the carbon by the melt-diffusion method. Finally, a double-shell carbon-coated CoFe nanoparticle ( $\text{CoFe@C}$ ) composite structure was rationally designed as sulfur hosts. Thanks to the unique chemical composition, the  $\text{CoFe@C}$  structure had many advantages, such as interior space to contain the volume expansion of sulfur and the formation of nanoparticles as well as a certain adsorption effect on polysulfide.

## 2. EXPERIMENTAL

### 2.1 Preparation of $\text{CoFe@C/S}$ composite

The  $\text{CoFe-PBA}$  nanocube was prepared as previously described [35]. Then, 15 mg of  $\text{CoFe-PBA}$  was dispersed uniformly into Tris buffer solution (10 mM, 100 mL) by sonication for 30 min. Then, 10

mg dopamine was added and stirred magnetically for 4 h. The sediment was collected by centrifugation, washed and dried to obtain the product CoFe-PBA@PDA. The CoFe-PBA@PDA nanocube was annealed in a N<sub>2</sub> atmosphere for 3 h at 500 °C to obtain CoFe@C. In a weight ratio of M<sub>S</sub>:M<sub>CoFe@C</sub> = 6:4, Sulfur and CoFe@C were mixed. The mixture was under a nitrogen atmosphere and pyrolysis at 155 °C for 12 h to prepare CoFe@C/S.

## 2.2 Characterization

X-ray diffraction (XRD, Japan Tsutsumi, D/MAX-3C) was conducted to analyze the and crystal microstructure. The FTIR(Perkon-Elmer 700, USA) and Raman spectroscopy (Andor SR-500i) have been carried out to characterize the chemical composition. The TGA/DSCI-type synchronous thermal analyzer was used to measure the sulfur content. The BET (NOVAtouch LX4) were utilized to the specific surface area, pore size distribution, and pore volume. The SEM (Hitachi, Japan, S-480) and TEM (TEM, JEOL JEM 2100) were used to analyze the structure and morphology. The x-ray photoelectron spectroscopy (XPS, Thermo ESCALAB 250XI) was conducted to assess the valence distribution of the elements.

## 2.3 Electrochemical measurement

The CoFe@C/S composite as an active material(70 wt%),conductive agent(20 wt%)and binder (PVDF, 10 wt%) was mixed. The mixture was uniformly spread on an aluminum foil, and then dried at 60 °C in a vacuum oven overnight. Nextly, using a tablet machine, the dried aluminum foil was cut into electrode pole pieces. The Celgard 2400 was used as separator and the lithium metal plate as the negative electrode. Further, the electrolyte is 1.0 mol/L LiTFSI/DME + DOL (1:1 by volume) with an appropriate amount of LiNO<sub>3</sub>. The CR2430 button battery was fabricated in an argon-filled glove box for next performance measurement. The Galvanostatic discharge/charge tests were performed at the Shanghai ChenHua CHI660D electrochemical workstation. The scanning range of CV was between 1.5 and 3.0 V with the scanning speed of 0.2 mV/s. The frequency ranges of AC impedance test was from 10<sup>-1</sup> Hz to 10<sup>5</sup> Hz. The Xinwei test system was used to measure at room temperature from 1.7 to 2.8 V.

## 3. RESULTS AND DISCUSSION

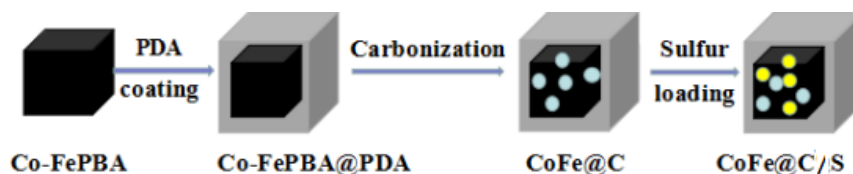


**Figure 1.** Schematic diagram of the preparation process of the CoFe@C/S composite.

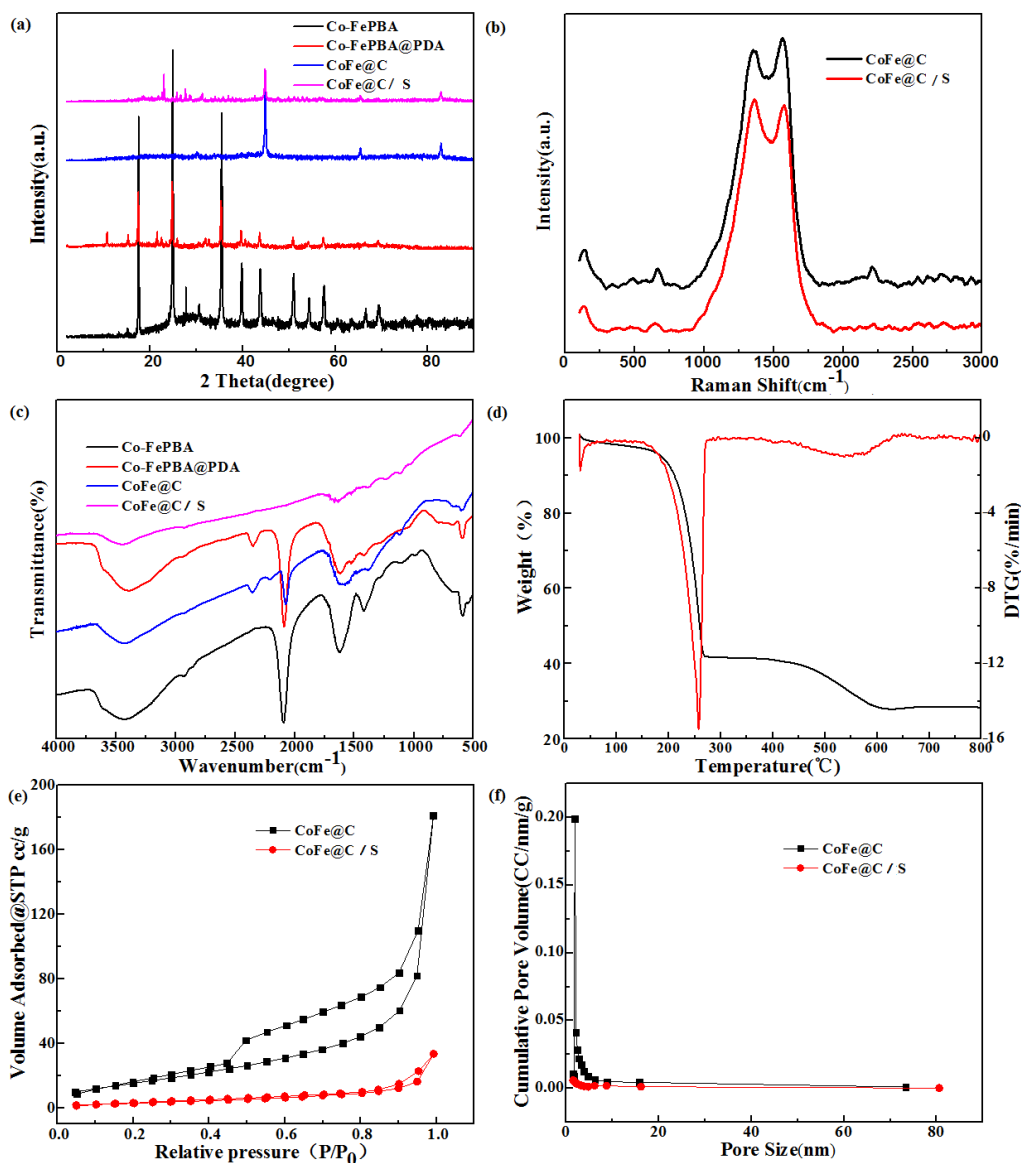


**Figure 2.** (a) XRD patterns of Co-FePBA, CoFe-PBA@PDA, CoFe@C, and CoFe@C/S composite. (b) Raman spectra patterns of CoFe@C and CoFe@C/S composites. (c) Fourier infrared spectra of Co-FePBA, CoFe-PBA@PDA, CoFe@C, and CoFe@C/S composites. (d) TG curve for the CoFe@C/S composite in nitrogen. (e) Nitrogen adsorption–desorption isotherm curves of CoFe@C and CoFe@C/S complexes. (f) Pore size distribution of CoFe@C and CoFe@C/S complexes.

The synthesis strategy of the CoFe@C/S composite is shown in Figure 1. First, we prepared uniform CoFe-PBA nanocubes by easy co-precipitation. Subsequently, the CoFe-PBA@PDA nanocube with a core-shell structure was formed by wrapping polydopamine (PDA) on the outward of the CoFe-PBA nanocube using Tris buffer solution. Next, the outer layer of PDA was calcined at 500°C and changed into N-doped carbon shell layer. In contrast, the inner layer of CoFe-PBA was converted into N-doped carbon-coated CoFeNP nanoparticles (CoFe@C). Finally, sulfur was impregnated into the voids of CoFe@C by the melt-diffusion method to obtain the final product CoFe@C/S.

Figure 2a shows the XRD patterns of the prepared four composites of CoFe-PBA, CoFe-PBA@PDA, CoFe@C, and CoFe@C/S. The diffraction peaks of the synthesized precursor CoFe-PBA at 17.5°, 24.8°, 30.5°, 35.4°, 39.8°, 43.8°, 51°, 54.3°, and 57.5° were consistent with previously reported data [35]. The peak was sharp and no other peaks appeared, indicating that the sample was of high crystallinity and purity. After coating the PDA, the peak of the CoFe-PBA@PDA complex significantly weakened. After carbonization at 500°C, the characteristic peaks at 31.3°, 44.9°, 65.4°, and 82.8° corresponded to the (100), (110), (200), and (211) crystal planes of the CoFe alloy structure, respectively. The feature peaks of orthogonal sulfur (JCPDS No.08-0247) and FeCo alloy (JCPDS No.65-6829) were detected in CoFe@C/S, indicating that sulfur was successfully incorporated into the composite and did not cause the rupture of old chemical bonds and the generation of new chemical bonds. Figure 2b shows the Raman spectra of CoFe@C and CoFe@C/S composites. The 1360 cm<sup>-1</sup> is the disordered D peak and the 1573 cm<sup>-1</sup> is the G peak in the spectrogram of the two samples. The intensity ratio of D peak to the G peak could be used to characterize the graphitization of the graphene sheet, and the smaller intensity reflected the higher degree of graphitization. The  $I_D/I_G$  value of CoFe@C/S composite is slightly higher than that of the CoFe@C complex, indicating that the CoFe@C/S had a higher defect density and could provide more electroactive sites to strengthen the electrochemical performance. FT-IR was conducted to determine the chemical group distribution and structural composition of the compound. Figure 2c shows the infrared absorption spectrum (FT-IR) of four composites of CoFe-PBA, CoFe-PBA@PDA, CoFe@C, and CoFe@C/S. A strong absorption peak was observed at 2080 cm<sup>-1</sup>, which corresponded to the stretching vibration of C≡N. And the two peaks at 501 and 601 cm<sup>-1</sup> correlated with two functional groups of Fe-CN-Fe and Fe-CN, respectively. The peaks at 1610 and 3535 cm<sup>-1</sup> corresponded to the OH bond, which was the characteristic peak of CoFe-PBA [36] and the successful indication of the synthesis of CoFe-PBA material. When dopamine was coated and carbonized, both these complexes had similar peaks similar to that of CoFe-PBA. However, the peak intensity weakened. After the final sulfur loading, the composite material did not show a distinct characteristic peak as a whole. Figure 2d shows a thermogravimetric difference thermal analysis curve of the CoFe@C/S composite measured in N<sub>2</sub>. The composite exhibited significant sample quality loss with an increase in temperature from 100°C to 270°C. The mass loss of this section arised from the loss of sulfur content. The curve remained almost parallel after the increase from 270°C to 400°C. The mass loss of the sample between 400°C and 600°C might occur possibly because of the combustion of the amorphous carbon material in the composite. The loss of sulfur content in the CoFe@C/S was about 59%.

Figure 2e and 2f show the BET results of CoFe@C and CoFe@C/S complexes. The isothermal curve of CoFe@C and CoFe@C/S complex belonged to the type IV isotherm in the IUPAC classification. Among these, the CoFe@C complex had a distinct H<sub>3</sub> hysteresis loop, which might be caused by uniform particle packing. The specific surface area of the CoFe@C composite was 105.6 m<sup>2</sup>/g. And the pore volume was 0.3 cm<sup>3</sup>/g. The CoFe@C composite could buffer the volume change in charge and discharge, simultaneously form the large open channel conductive to electrolyte penetration, and speed up the migration rate of Li<sup>+</sup>/e<sup>-</sup>. The average pore diameter of the CoFe@C composite was about 1.9 nm, and the largest pore diameter reached about 75 nm, indicating that the composite had mesopores and macropores coexisting. However, the specific surface area was reduced to 12.4 m<sup>2</sup>/g, and the pore volume of the CoFe@C/S composite lowered to 0.05 cm<sup>3</sup>/g, respectively, indicating successful sulfur

diffusion into the host material.

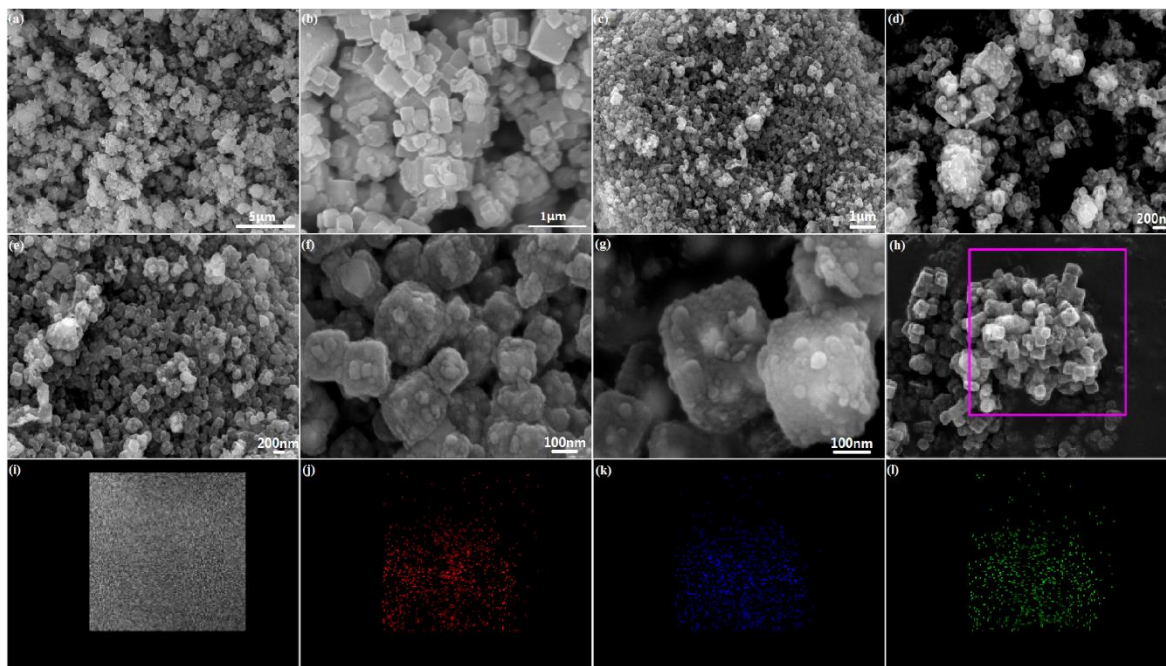


**Figure 3.** SEM images of (a and b) the Co-Fe PBA nanocubes and (c – g) CoFe@C/S composite and (h) the SEM images and the corresponding EDX mappings of (i–l) the CoFe@C/S composite.

The structure and form of the samples were examined using SEM. In Figure 3a and 3b, the distribution of the CoFe-PBA nanocube was uniform, with a smooth surface and no obvious agglomeration. The average size was about 500 nm. Figure 3c – 3g are SEM images of the sulfur after loading. Obviously, the morphology of the material was well maintained and no excessive sulfur particles were observed outside, indicating the successful diffusion of sulfur into the nanocube. The large space in the carbon shell accommodated not only high-load sulfur but also sulfur volume expansion during the process of lithiation. The strong chemical interaction between polar CoFe nanoparticles and polysulfides allowed the anchoring and retention of most part of polysulfides in the double-shell carbon. EDX element mapping analysis was performed on CoFe@C@S composites to prove the existence of Co, Fe, C, and S elements (Fig. 3h). As shown in Figure 3 i–l, Co, Fe, C, and S elements were uniformly dispersed.

The TEM (Fig.4a and 4b) images demonstrated that the visible coated dopamine was clearly observed outside the CoFe-PBA, and the size of the CoFe-PBA nanocube encapsulated by dopamine increased to about 200 nm; the thickness of the carbon shell was around 10 nm. The double-shelled carbon was evident in the SEM and TEM images.

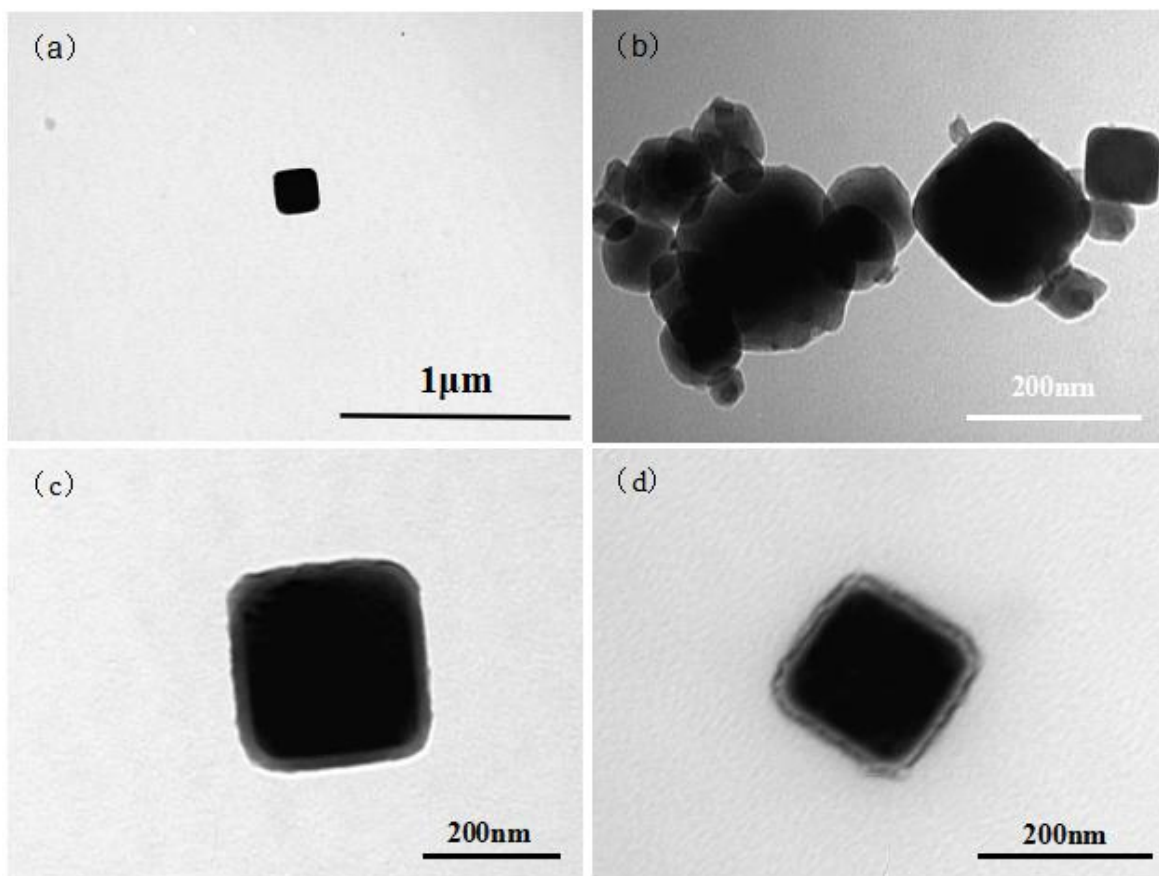


**Figure 4.** TEM images of (a and b) the CoFe-PBA, (c) CoFe-PBA@PDA, and (d) CoFe@C .

The size of the cube significantly increased after the PDA was coated in the SEM image, and the two carbon shells were clearly seen in the TEM image. These dopamine-coated CoFe-PBA nanocubes were then converted into double-shell carbon-coated CoFe nanoparticles after annealing in an  $N_2$  atmosphere at  $500^\circ C$ . The nitrogen-doped carbon shell generated after dopamine carbonization served as a nanoscale electrochemical reaction chamber and provided the physical boundary for diffused polysulfide. Figure 4c and 4d shows that the structure of the nanocube was maintained after carbonization of the composite, and the outermost carbon shell was seen clearly. Therefore, we could infer that the outside of CoFe-PBA was successfully wrapped by the dopamine layer. Both polar CoFe nanoparticles and carbon shells accelerated the electronic transmission and electrochemical reaction kinetics. The synergy of the two sessions showed an excellent specific capacity and cyclic stability while serving as the positive anode in Li-S batteries.

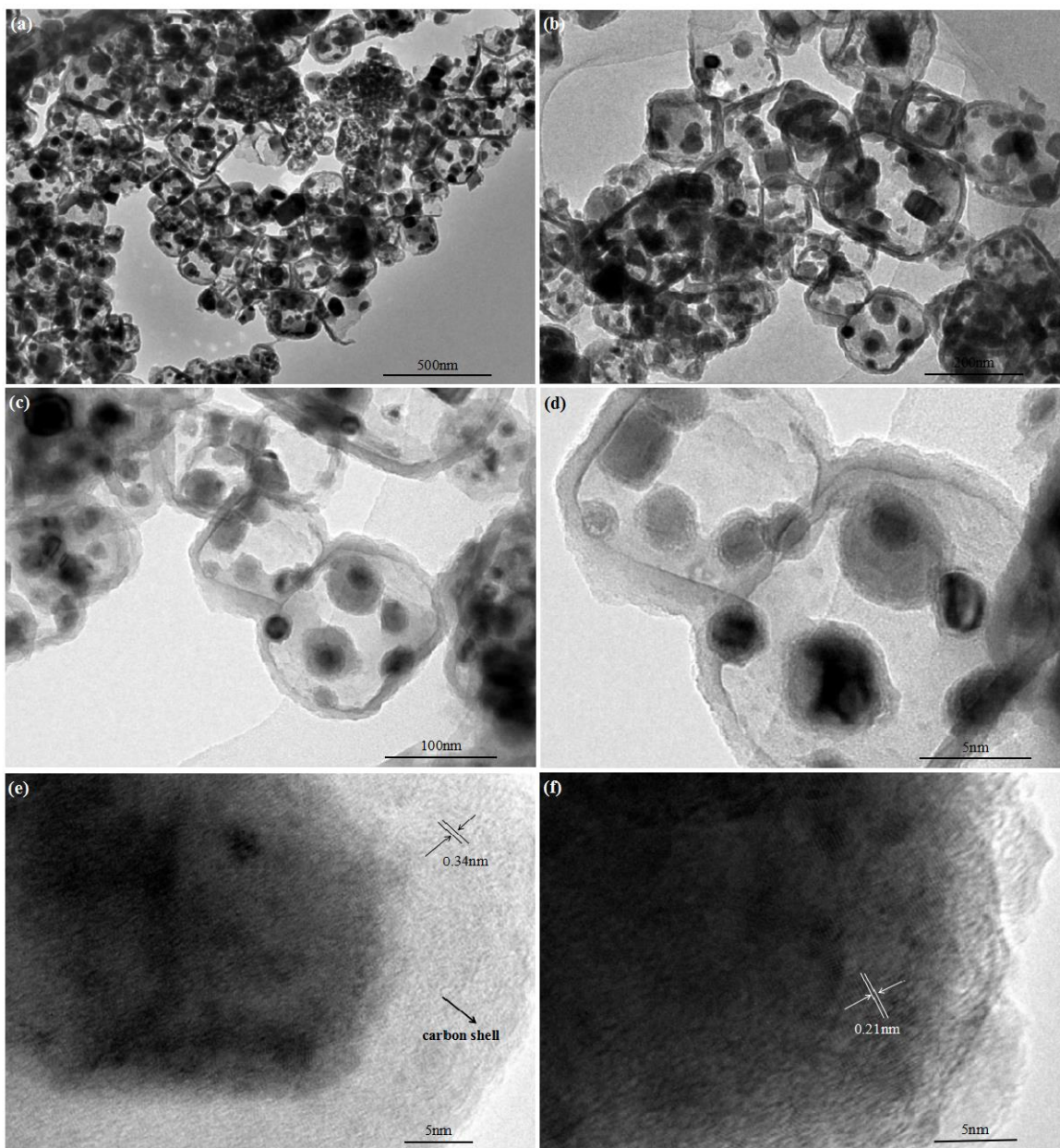


**Figure 5.** TEM images of CoFe@C/S composites. (a and b) Low-magnification images, (c and d) high-magnification images, and (e and f) HRTEM images.

Figure 5a - 5d shows that the CoFe@C/S composite exhibited a unique double-shell nanocube structure in TEM images at different magnifications. A certain space existed in the double-shell carbon layer, which could adapt to the sulfur volume expansion during charging and discharging. Meanwhile, sulfur was uniformly dispersed in the main body, and no obvious agglomeration was observed. Figure 5 shows that FeCo particles were located on the surface and voids inside the carbon shell, and the average size was about 10 nm. The main purpose of FeCo nanoparticles was to take in polysulfides and restrain the shuttle of polysulfides in the electrolyte. The HRTEM images in Figure 5e and 5f show that the lattice fringe spacing of carbon material and CoFe particles was about 0.34 and 0.21 nm, corresponding to the (002) and (110) crystal plane spacing, respectively [37].

The surface chemical composition and state of the synthesized CoFe@C composites were then investigated by XPS.

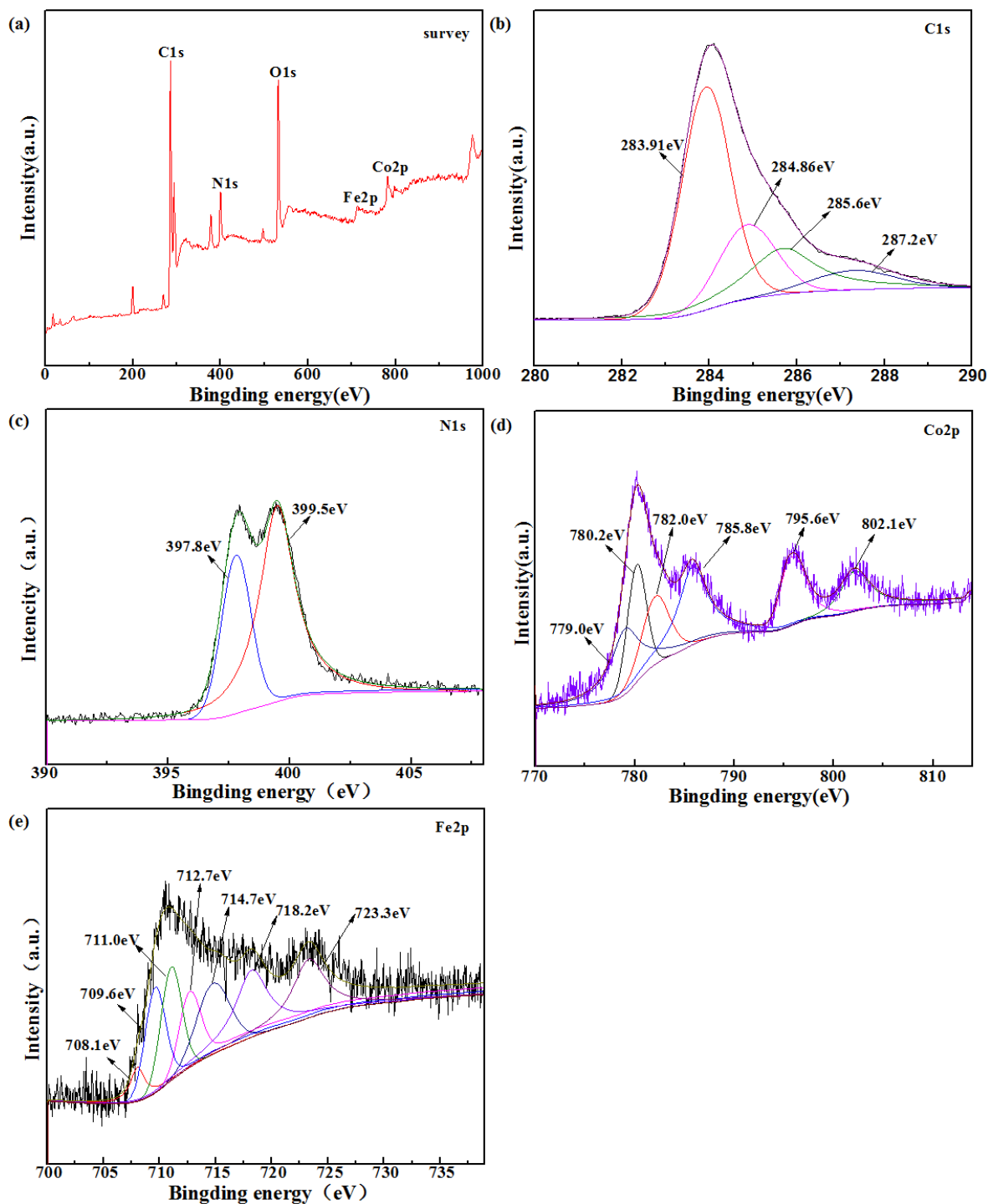


**Figure 6.** The XPS spectra of (a) survey, (b) N1s, (c) C 1s , (d) Co2p and (e) Fe2p for CoFe@C composites.

As shown in Figure 6, the XPS spectrum of CoFe@C, the composite clearly proved that the material contained five elements: C (284.26 eV), N (398.80 eV), O (530.95 eV), Fe (710.80 eV), and Co

(780.70 eV), indicating that the N atom was successfully doped into the carbon material. The XPS spectrum of N1s (Fig.6b) showed that the two peaks at 397.8 and 399.5eV were ascribed to pyridine-type and pyrrole-type nitrogen, respectively.

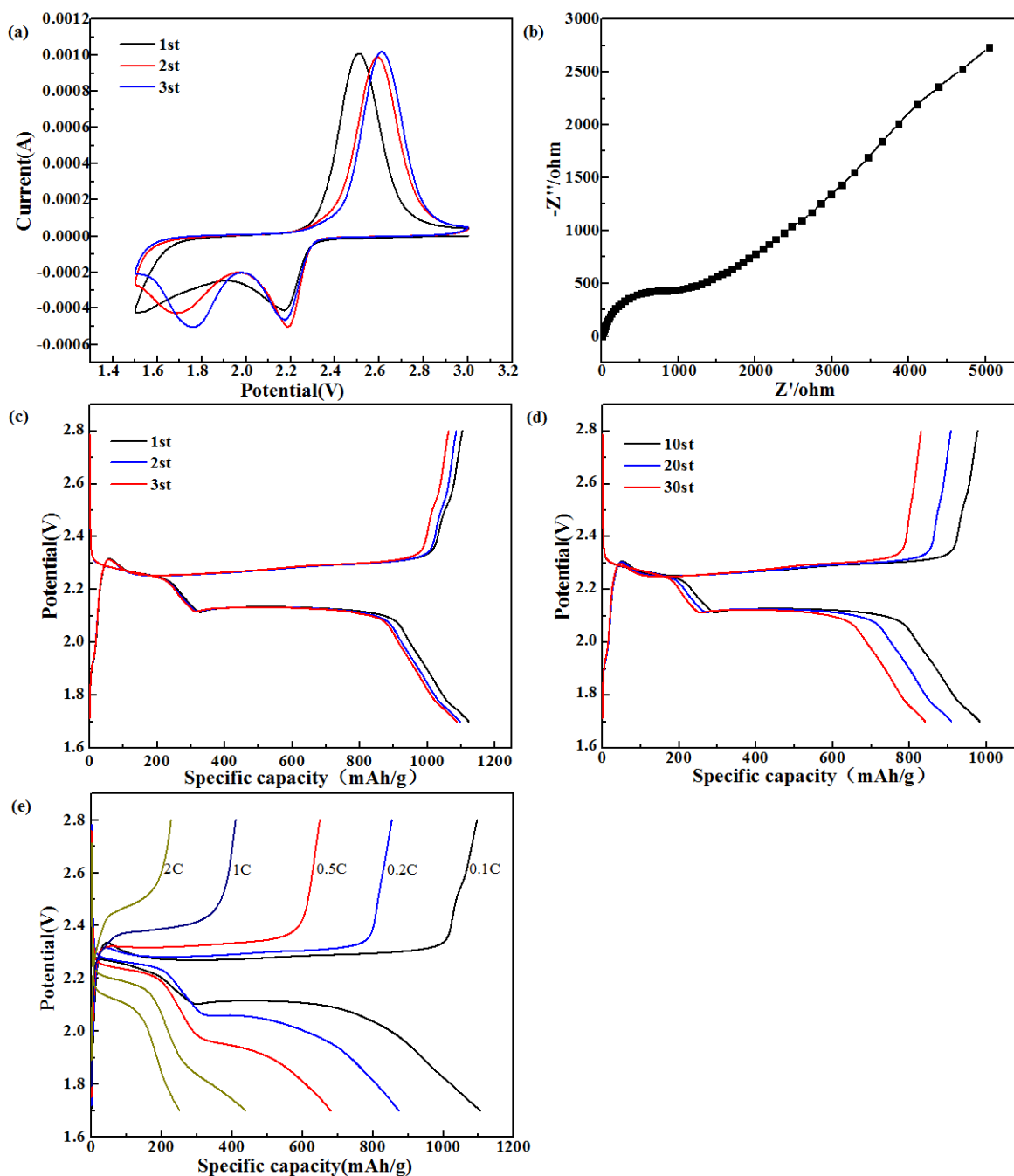


**Figure 7.** Cyclic voltammety curve (a) of the CoFe@C/S composite at a scan rate of  $0.2 \text{ mVs}^{-1}$ , the electrochemical impedance spectroscopy (b) of the CoFe@C/S composite, and the typical voltage profiles of the CoFe@C/S composite electrode at 0.1 C. (c) The first three turns and (d) the 10th, 20th, and 30th cycles, and (e) the first charge–discharge curve of the CoFe@C/S composite electrode at 0.1 C, 0.2 C, 0.5 C, 1 C, and 2 C.

These two types of nitrogen can increase the conductivity of carbon materials. The XPS spectrum of C1s (Fig. 6c) was deconvoluted into four contributions, with peaks at 283.9 eV, 284.8 eV, 285.6 eV, and 287.2 eV associated with C—C, C—N, C—O, and C = O, respectively [38]. In Fig. 6d, the Co 2p spectrum showed three kind of Co species, which was consistent with the metals Co (778.6 eV), Co<sub>x</sub>O<sub>y</sub> (780.2 and 795.9 eV), and Co-N<sub>x</sub> (782.6 eV), and confirmed the formation of Co-N bonds[39]. This was the satellite peak at 786.8 and 803.1 eV. Figure 6e shows the Fe2p spectrum. The peak at 708.0 eV corresponded to the metal Fe and the peaks at 709.6, 712.7, and 723.3 eV corresponded to different iron oxides[40]. The peak at 711.3 eV corresponded to FeN<sub>x</sub>, which confirmed the formation of Fe-N bonds [41].

We tested the CV curve for the first three turns of the CoFe@C/S composite with a voltage range of 1.5 – 3V and a scan rate of 0.2mV s<sup>-1</sup> to illustrate the influence of the CoFe@C/S composite on the redox reaction of LiPS. As shown in Figure 7a, two major cathode peaks and one anode peak were clearly visible after the first, second, and third cycles. The peaks located at about 2.2 corresponded to the translation process from the elemental sulfur to long-chain lithium polysulfide. The peaks located at about 1.8 V was attributed to the transformation process of long-chain lithium polysulfide into short-chain lithium polysulfide (Li<sub>2</sub>S<sub>2</sub>/Li<sub>2</sub>S). Located near 2.6 V, the only oxidation peak was owing to the transition from short-chain insoluble Li<sub>2</sub>S and Li<sub>2</sub>S<sub>2</sub> to S<sub>8</sub>. In addition, the cyclic voltammetry curves from the first to the third circle gradually overlapped. So, it is possible to budget the composite electrode for good reversibility.

Next, the electrochemical behavior of the CoFe@C/S composite was studied using EIS. Figure 7b shows the impedance performance curve of the CoFe@C/S composite after five cycles of CV. The Nyquist plot was composed of two parts: one is a flat semicircle at high frequencies, and the other is a diagonal line at low frequencies. The semicircle represented the charge transfer resistance and contact resistance, and the oblique line represented the Warburg resistor, which had relations with the diffusion of lithium ions. The figure shows that the CoFe@C/S composite had a smaller semicircle diameter and a larger slope, indicating that the CoFe@C/S composite had lower resistance and faster ion transport.

Then, the galvanostatic charge/discharge (GCD) curves at voltage range of 1.7 and 2.8 V at 0.1 C were further carried out to analyze the electrical energy storage property. Figure 7c and 7d shows the GCD curves of CoFe@C/S electrodes. From the GCD curve, it can be clearly seen that there are two discharge platforms and one charging platform, which coincided with those in the CV curve. All of the GCD curves withstood two distinct plateaus at 2.3 and 2.1 V (vs Li<sup>+</sup>/Li), which were categorized as the following two stages:[42-44]

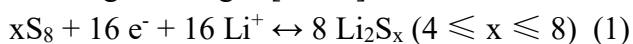
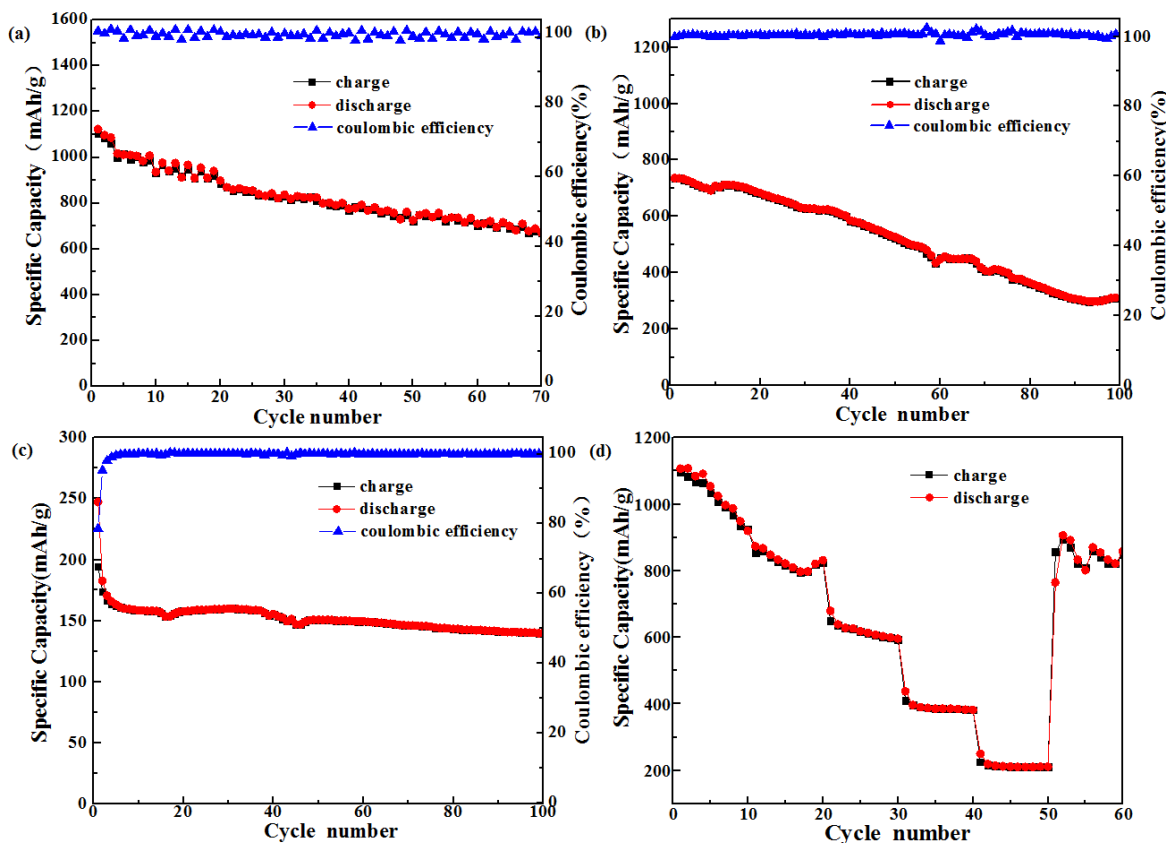


Figure 7e shows the GCD voltage profiles even at high current density. Two typical discharge and one charging platforms could be observed, indicating lower polarization. Therefore, the CoFe@C/S composite was used as the cathode material of Li-S battery, which could effectively reduce the volume expansion and accumulation of sulfur during the charging and discharging process to achieve high capacity and a higher sulfur utilization rate, and ensure the cycle stability of the electrode.



**Figure 8.** Cycling performance and the coulombic efficiency of the CoFe@C/S electrode at (a) 0.1 C (b) 0.5 C, and (c) 2 C. (d) Rate performance of the CoFe@C/S electrode.

Next, we evaluated the electrochemical performance of CoFe@C/S composites at different current densities. The initial specific discharge capacity of the CoFe@C/S composite was  $874.4 \text{ mAhg}^{-1}$  at 0.1C. Also, the charge-specific capacity was as high as  $1105.3 \text{ mAhg}^{-1}$ , which was attributed to the formation of electrolyte SEI film and the internal resistance of the battery change during the first charge and discharge. During the first few cycles, the volume expansion and redistribution of active sulfur might lead to rapid capacity degradation. Even with rapid capacity decay, the high coulombic efficiency indicated that the CoFe@C/S composite effectively mitigated the polysulfide dissolution into the organic electrolyte. In the CoFe@C/S composite material, the large space in the carbon shell buffered the volume expansion of sulfur to a certain extent, which enabled the rapid redistribution of sulfur species, while also avoiding the structural collapse of the host material. CoFe nanoparticles could take in polysulfides, suppress the shuttle effect of polysulfides, and prevent the depletion of positive and negative active materials. As shown in Figure 8b, the high capacity of  $311.1 \text{ mAhg}^{-1}$  and a high coulombic efficiency of more than 98% were maintained after 100-time charge and discharge cycles at the current density of 0.5 C. More importantly, as shown in Figure 8c, the stable cycle performance was maintained after 100 cycles at 2 C, the battery capacity still retain  $140.1 \text{ mAhg}^{-1}$ , and the coulombic efficiency per cycle was about 99%. The rate capability of the CoFe@C/S composite was also evaluated by cycling when the current densities changed from 0.1 C to 2 C and then resumed to 0.1 C (Fig. 8d). The first discharge capacity of the electrode at 0.1 C, 0.2 C, 0.5 C, 1 C, and 2 C provided capacities of 1106.3, 873.6, 679.8,

438.0, and 250.6 mAhg<sup>-1</sup>, respectively, further confirming excellent electron/ion transport properties and improved reaction kinetics. When the current density was switched back to 0.1 C, the electrode capacity was still exceedingly recovered, which is higher than other materials under the same conditions. As Table 1 shows, compared with the other metal-carbon composites for Li-S battery, the battery performance with CoFe@C cathode is equivalent or higher than, particularly in terms of cyclic stability. This indicated that the structure of the CoFe@C/S composite had excellent stability and cyclic reversibility.

**Table 1.** Comparison of Li-S performance of CoFe@C with reported results.

Sample	Initial capacity (mAh g <sup>-1</sup> , at n C)	Reversible capacity (mAh g <sup>-1</sup> )	Ref.
CoFe@C	1105.3 (0.1 C)	568.6 (0.1C, 100th)	This work
S/CoFe@NC/ PPC	1049 (0.1 C)	408.9 (0.1C, 200th)	[45]
CoO/SnO <sub>2</sub> @NC/S	395.7 (0.2 C)	302.7 (0.2C, 400th)	[46]
the Co@NCNTs-2-S	578 (0.5 C)	461 (0.5C, 300th)	[47]
S@Fe-Ni@NC	900(0.1 C)	268.5(0.1C, 500th)	[48]

#### 4. CONCLUSIONS

In conclusion, we designed a composite structure of double-shell carbon-coated CoFe nanoparticles as a sulfur host material. This kind of structure benefited from the double-shell carbon and CoFe nanoparticles. First, the double-shell carbon could ensure superior electrical conductivity for the electrode, and the nitrogen-doped carbon could effectively adsorb lithium polysulfide. Second, the inner cavum construction of the carbon material itself could also restrict the polysulfide dissolution process and accommodate the sulfur volume expansion. Finally, polysulfides could be strongly adsorbed by CoFe nanoparticles, and could efficiently impede them from dissolving in the course of charge and discharge. The sulfur content of CoFe@C composite electrode reached 59 wt% using this effective improvement measure. After 100 cycles at 0.1 C, the capacity was still 568.6 mAhg<sup>-1</sup>. When the density reaches 2 C, the reversible capacity was still 140.1 mAhg<sup>-1</sup> after 100 cycles, the coulombic efficiency was maintained above 99%, and the capacity retention rate was 56.7%.

#### ACKNOWLEDGEMENTS

This work is supported by the Fundamental Research Program of Shanxi Province (Grant No. 202103021223201), National Natural Science Foundation of China (Grant No. 52175554), and the Scientific and Technological Innovation Programs of Higher Education Institutions in Shanxi (Grant No. 2019L0606).

#### References

1. X. L. Fan, Y. Q. Liu, J. Y. Tan, S. Yang, X. Y. Zhang, B. L. Liu, H. M. Cheng, Z. H. Sun and F. Li, *J. Mater. Chem. A*, 10(2022)7653.

2. D. Muthuraj, R. Murugan, P. R. Rayappan, G. R. Kandregula and K. Ramanujam, *New J. Chem.*, 46(2022)3185.
3. M. Yan, H. Chen, Y. Yu, H. Zhao, C. F. Li, Z. Y. Hu, P. Wu, L. Chen, H. Wang, D. Peng, H. Gao, T. Hasan, Y. Li and B. L. Su, *Adv. Energy Mater.*, 8(2018)1801066.
4. Y. Xiao, Z. Yi, H. Zeng, W. Zhang, B. Tian and Y. Deng, *J. Alloy. Compd.*, 787 (2019)1356.
5. B. Kalimuthu, N. Muralidharan and K. Nallathamby, *J. Alloy. Compd.*, 780(2019)177.
6. W. Yang, W. Yang, L. B. Dong, X. C. Gao, G. X. Wang and G. J. Shao, *J. Mater. Chem. A*, 7(2019)13103.
7. S. S. Zhang, *Inorg. Chem. Front.*, 2(2015)1059.
8. X. Liu, J. Q. Huang, Q. Zhang and L. Mai, *Adv. Mater.*, 29(2017) 1601759.
9. Y. Y. Gui, P. Chen, D. Y. Liu, Y. Fan, J. Zhou, J. X. Zhao, H. Liu, X. Guo, W. Q. Liu and Y. Cheng, *J. Alloy Compd.*, 895(2022)162495.
10. Y. H. Seon, R. Saroha and J. S. Cho, *Compos. Part B-Eng.*, 237(2022)109856.
11. Y. Zhang, L. Ma, R. X. Tang, F. F. Zhao, S. L. Niu, W. D. Su, C. Pan and L. M. Wei, *Appl. Surf. Sci.*, 585(2022)152498.
12. M. T. Liu, S. Jhulki, Z. F. Sun, A. Magasinski, C. Hendrix and G. Yushin, *Nano Energy*, 79(2021)105428.
13. H. Zhang, Q. M. Gao, Z. Y. Li, P. Xu, H. Xiao, T. F. Zhang and X. Liang, *Electrochim. Acta*, 343(2020)136079.
14. R. Saroha, J. H. Oh, J. S. Lee, Y. C. Kang, S. M. Jeong, D. W. Kang, C. Cho and J. S. Cho, *Chem. Eng. J.*, 426(2021)130805.
15. H. Ahn, Y. Kim, J. Bae, Y. K. Kim and W. B. Kim, *Chem. Eng. J.*, 401(2020)126042.
16. Y. S. Zhang, P. Zhang, B. Li, S. J. Zhang, K. L. Liu, R. H. Hou, X. L. Zhang, S. R. P. Silva and G. S. Shao, *Energy Storage Mater.*, 27(2020)159.
17. Z. X. Cao, J. Guo, S. N. Chen, Z. N. Zhang, Z. P. Shi, Y. H. Yin, M. G. Yang, X. X. Wang and S. T. Yang, *J. Mater. Chem. A*, 9(2021) 21867.
18. F. Zhou, Z. Li, X. Luo, T. Wu, B. Jiang, L. L. Lu, H. B. Yao, M. Antonietti and S. H. Yu, *Nano Lett.*, 18(2018)1035.
19. L. W. Shi, M. M. Cheng, W. Q. Zhang and S. F. Hou, *Mater. Lett.*, 301(2021)130332.
20. J. Zhao, Y. Y. Zhao, W. C. Yue, X. Li, N. Gao, Y. J. Zhang and C. Q. Hu, *Chem. Eng. J.*, 441(2022)136082.
21. E. D. Jing, L. Chen, S. D. Xu, W. Z. Tian, D. Zhang, N. N. Wang, Z. C. Bai, X. X. Zhou, S. B. Liu, D. H. Duan and X. Y. Qiu, *J. Energy Chem.*, 64(2022)574-582.
22. N. Zhang, S. S. Zheng, M. L. Zhao, Y. Lu, J. B. Cheng, Y. Yang, T. Peng and Y. S. Luo, *Dalton Trans.*, 50(2021)17120.
23. Q. Cheng, Z. X. Pan, H. S. Rao and X. H. Zhong, *J. Alloy. Compd.*, 901(2022)163625.
24. J. B. Liu, Z. S. Qiao, Q. S. Xie, D. L. Peng and R. J. Xie, *ACS Appl. Mater. Interfaces*, 13(2021)15226.
25. M. A. Al-Tahan, Y. T. Dong, A. E. Shreshr, X. B. Liu, R. Zhang, H. Guan, X. Y. Kang, R. P. Wei and J. M. Zhang, *J. Colloid Interf. Sci.*, 609(2022)235.
26. G. Babu, M. Masurkar, H. Al Salem and L. M. R. Arava, *J. Am. Chem. Soc.*, 139 (2017)171.
27. J. F. Wang and J. Li, *J. Colloid Interf. Sci.*, 616(2022)298.
28. H. Peng, Y. G. Zhang, Y. L. Chen, J. Zhang, H. Jiang, X. Chen, Z. G. Zhang, Y. B. Zeng, B. S. Sa, Q. L. Wei, J. Lin and H. Guo, *Mater. Today Energy*, 18(2020)100519.
29. L. J. Yu, Y. D. Qu, R. X. Dang, Z. K. Ma, L. F. Duan and W. Lü, *Electroanal. Chem.*, 907(2022)116025.
30. M. S. Garapati and R. Sundara, *ACS Omega* 5(2020)22379.
31. L. M. Jin, J. Ni, C. Shen, F. L. Peng, Q. Wu, D. H. Ye, J. S. Zheng, G. R. Li, C. M. Zhang, Z. P. Li and J. P. Zheng, *J. Power Sources*, 448(2020)227336.
32. Y. Z. Wang, D. Adekoya, J. Q. Sun, T. Y. Tang, H. L. Qiu, L. Xu, S. Q. Zhang and Y. L. Hou, *Adv.*

- Funct. Mater.*, 29 (2018)1807485.
33. D. W. Su, M. Cortie, H. B. Fan and G. X. Wang, *Adv. Mater.*, 29(2017)1700587.
34. X. Wu, L. S. Fan, Y. Qiu, M. Wang, J. Cheng, B. Guan, Z. Guo, N. Zhang and K. Sun, *Chem. Sus. Chem.*, 11 (2018)3345.
35. L. M. Cao, Y. W. Hu, S. F. Tang, A. Iijin, J. W. Wang, Z. M. Zang and T. B. Lu, *Adv. Sci.*, 5 (2018)1800949.
36. V. Escax, A. Bleuzen, C. Cartier dit Moulin, F. Villain, A. Goujon, F. Varret and M. Verdaguer, *J. Am. Chem. Soc.*, 123(2001)12536.
37. W. T. Qi, W. J. Wu, B. Q. Cao, Y. Zhang and Y. C. Wu, *Int.J. Hydrogen Energ.*, 44 (2019) 20257.
38. Q. Hu, G. M. Li, G. D. Li, X. F. Liu, B. Zhu, X. Y. Chai, Q. L. Zhang, J. H. Liu and C. X. He, *Adv. Energy Mater.*, 9(2019)1803867.
39. M. Li, S. Chen, B. Li, Y. Q. Huang, X. W. Lv, Panpan Sun, L. Fang, X. H. Sun, *Electrochimica Acta.*, 388 (2021) 138587
40. F. Wang, Z. X. Xiao, X. Liu, J. W. Ren, T. Xing, Z. Li, X. Y. Li and Y. L. Chen, *J. Power Sources*, 521 (2022) 230925
41. Q. Hu, G. M. Li, G. D. Li, X. F. Liu, B. Zhu, X. Y. Chai, Q. L. Zhang, J. H. Liu and C. X. He, *Adv. Energy Mater.*, 9(2019)1803867.
42. L. Hu, C. Dai, H. Liu, Y. Li, B. Shen, Y. Chen, S.-J. Bao and M. Xu, *Adv. Energy Mater.*, 8 (2018) 1800709.
43. X. Ji, K. T. Lee and L. F. Nazar, *Nat. Mater.*, 8 (2009) 500–506.
44. S. Fan, S. Huang, M. E. Pam, S. Chen, Q. Wu, J. Hu, Y. Wang, L. K. Ang, C. Yan, Y. Shi and H. Y. Yang, *Small*, 15 (2019) 1906132.
45. S. Jing, P. Ding, Y. L. Zhang, H. G. Liang, S. B. Yin, P. Tsiakaras, *Ionics*, 25(2019) 5297–5304.
46. M. T. Duan, M. R. Wu, K. Xue, Z. X. Bian, J. Shi, X. M. Guo, F. Cao, J. H. Zhang, Q. H. Kong and F. Zhang, *Int. J. Miner. Metall. Mater.*, 28(2021)1647.
47. C. Qi, S. Zu, X. Zhu, T. Zhang, L. Li, L. Song, Y. C. Jin, M. D. Zhang, *Appl. Surf. Sci.*, 601 (2022) 154245.
48. C. Song, Q. W. Jin, W. Zhang, C. C. Hu, Z. Bakenov, Y. Zhao, *J. Colloid Interf. Sci.*, 595 (2021) 51.